Contents lists available at ScienceDirect

Combustion and Flame

journal homepage: www.elsevier.com/locate/combustflame

Effect of packing density on flame propagation of nickel-coated aluminum particles

Dilip Srinivas Sundaram, Vigor Yang *

School of Aerospace Engineering, Georgia Institute of Technology, Atlanta, GA 30032, USA

ABSTRACT

The combustion-wave propagation of nickel-coated aluminum particles is studied theoretically for packing densities in the range of 10–100% of the theoretical maximum density. Emphasis is placed on the effect of packing density on the burning properties. The energy conservation equation is solved numerically and the burning rate is determined by tracking the position of the flame front. Atomic diffusion coefficients and reaction rate of isolated nickel-coated aluminum particles are input parameters to the model. The burning behaviors and combustion wave structures are dictated by the heat transfer from the flame zone to the unburned region. Five different models for the effective thermal conductivity of the mixture are employed. The impact of radiation heat transfer is also assessed. As a specific example, the case with a particle size of 79 μm is considered in detail. The burning rate remains nearly constant (<1 cm/s) up to a packing density of 60%, and then increases sharply toward the maximum value of 11.55 cm/s at a density of 100%. The Maxwell–Eucken–Bruggeman model of thermal conductivity offers the most accurate predictions of the burning rate for all loading densities.

1. Introduction

Aluminum particles with diameters greater than 100 μm ignite only upon melting of the amorphous aluminum oxide (Al_2O_3) layer at 2350 K [1]. The particle ignition characteristics can be significantly enhanced by substituting a nickel coating for the oxide layer [1]. For example, the ignition temperature of ∼2.5 mm nickel-coated aluminum particles is ∼1600 K, which is substantially lower than the melting point of aluminum oxide [2]. This phenomenon is attributed to the presence of exothermic reactions between nickel and aluminum atoms [2,3]. The flame speed of micron-sized particle dust clouds can be quadrupled by employing nickel-clad aluminum particles [4]. At nano scales, nickel coating may be used to enhance the active aluminum content of the particle [5]. As a result, nickel-coated aluminum particles have been studied for propulsion and energy-conversion applications [1–5].

Combustion synthesis is an attractive method for manufacturing nickel aluminides (Ni_xAl_{1-x}), which are advanced structural materials for a variety of engineering systems [6,7]. The adiabatic reaction temperature of a nickel–aluminum system is as high as 1910 K [8], considerably greater than those achieved in conventional methods. The high temperatures drive out volatile impurities, producing relatively pure materials. The process can be operated in two modes. In the propagation mode [9,10], the powder is ignited at one end and a self-sustaining combustion wave propagates through the unburned mixture. The thermal explosion mode, which is applicable for systems with low exothermicity, involves heating the entire sample to the ignition temperature [11,12]. The reactant pellet is typically obtained by compacting the powder in a die using a hydraulic press [13].

Recently, the cold spray method has been employed to synthesize fully dense energetic materials [13]. The particles were entrained in a carrier gas and accelerated through a de Laval nozzle and directed to a substrate. The primary advantage of this method is the low process temperature, which helps to minimize reactions during deposition. Unlike a cold pressing technique, the product density is relatively uniform in both radial and axial directions [13]. The starting material may consist of nickel and aluminum particles or nickel-coated aluminum particles [12,13]. Understanding their burning properties is thus of paramount importance for material synthesis applications.

The physicochemical behaviors of nickel–aluminum systems has been extensively studied by means of experiments [2,10,11–14] and molecular dynamics (MD) simulations [3,15–17]. The materials of interest include multi-layered foils [11,15], core–shell structured particles [3,12–14,16], and consolidated blends of nickel and aluminum particles [10,12,13]. The reactivity of Ni–Al systems

* Corresponding author. Fax: +1 404 894 2760.
E-mail address: vigor.yang@aerospace.gatech.edu (V. Yang).

Nomenclature

c	burning-time constant
C_p	specific heat
D	pellet diameter, diffusion coefficient
d_p	particle diameter
E_A	activation energy
h	heat transfer coefficient
k	imaginary part of refractive index
K_0	frequency factor
L	pellet length
l_0	optical thickness
n	real part of refractive index
Q_a	absorption efficiency
Q_{conv}	convective heat transfer rate
Q_{gen}	heat generation rate
Q_r	heat of reaction
Q_{rad}	radiative heat transfer rate
Q_s	scattering efficiency
r	core radius
R	particle radius, universal gas constant
T	temperature
t	time
t_b	burning time
x	spatial coordinate

Greek

α	volume fraction
ρ	density
λ	thermal conductivity, wavelength
ε	emissivity
σ	Stefan–Boltzmann constant
$\dot{\omega}$	reaction rate
ϕ	volume fraction
β	extinction coefficient
η	fraction of burned reactants

Subscripts

a	ambient
f	fluid, flame
ign	ignition
m	mixture
P	preheat zone
p	particle
R	reaction zone
r	radiation
u	unburned
1	Maxwell–Eucken structure

is facilitated by melting of aluminum [2,11,12], although reactions have also been observed to occur at temperatures substantially lower than the melting point of aluminum (933 K) [18,19]. The predominant reaction pathway is the dissolution (or diffusion) of nickel atoms in liquid aluminum, formation of various inter-metallic phases at the interface, and precipitation of NiAl, a highly exothermic process [2,11]. Table 1 shows the heat of formation of several Ni–Al compounds [6]. NiAl has the highest heat of formation on a per mol-atom basis. Ignition may be caused by melting of eutectic mixture (Al–NiAl$_3$) [12], intermediate product (e.g. NiAl$_3$ or Ni$_2$Al$_3$) [12] or formation of NiAl [2]. The melting temperatures of different Ni–Al alloys are also given in Table 1. For nickel-coated aluminum particles, mechanical fracture of nickel shell may further assist the ignition process [12,16]. It is important to recognize that the ignition behavior of isolated particles could be different from that of powder compacts, due to the effects of heat losses and collective phenomenon [2]. The reactivity can be enhanced by both thermal and mechanical stimuli [14].

The flame propagation characteristics of Ni–Al multi-layered foils [20–22] and particulate systems [10,13,23,24] have been widely studied, while those of nickel-coated aluminum particles are yet to be understood. Dean et al. [13], recently, measured the burning rates of pressed and cold sprayed nickel–aluminum samples over a density range of 55–100% of the theoretical maximum density (TMD). For pellets containing nickel and aluminum particles, the burning rate decreases with increasing pellet density. An opposite trend was, however, observed for nickel-coated

aluminum particles. Samples with densities lower than 55% of the theoretical maximum density (TMD) were not considered, since they were mechanically unstable. It is apparent that the effect of packing density on burning properties of nickel-coated aluminum particles needs to be further explored. The present work aims to address this issue for densities in the range of 10–100% TMD. Five different models for the effective thermal conductivity of the mixture are employed. The model that accurately captures the measured variations of the burning rate with packing density is then determined.

2. Theoretical framework

The theoretical analysis treats one-dimensional and planar flame propagation of a uniformly packed pellet of nickel-coated aluminum particles in an argon environment. In reality, non-uniform packing of particles often takes place and results in density

Table 1
Heat of formation and melting point of Ni–Al inter-metallic compounds [2,6].

Species	Heat of formation, kJ/mol	Melting point, K
NiAl$_3$	−150.624	1127
Ni$_2$Al$_3$	−282.42	1406
NiAl	−118.4	1910
Ni$_3$Al	−153.134	1668
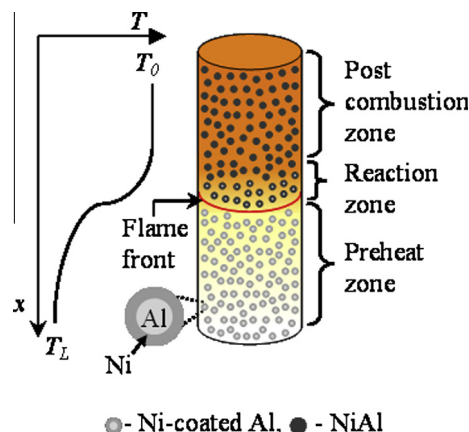
Fig. 1. Schematic of the physical model of flame propagation of nickel-coated aluminum particles.

gradients in both the radial and axial directions [13]. Furthermore, degassing of particles causes the pellet to expand and deform during combustion. The velocity of the flame front may thus not be constant throughout the burning process. To good approximation, nonetheless, particles are assumed to be uniformly packed and degassing is neglected. Figure 1 shows the physical model considered in the study. The particles are assumed to be uniformly sized and their agglomeration is neglected. The interstitial spaces between the particles are filled with argon gas. Following common practice, the entire region of interest is divided into preheat, reaction, and post combustion zones. The presence of chemical reactions is neglected in the preheat zone. The particles begin to react only when the local temperature reaches the ignition point, T_{ign}. Heat losses to the ambient environment by convection and radiation are taken into account. Mass and energy balances are enforced for a differential element and the resulting conservation equations are solved to obtain the burning rate and temperature distribution. Table 2 summarizes the thermophysical properties of different species at 1 atm. The initial temperature is 298 K. The properties of argon are taken from Ref. [25], while those of Al, Ni, and NiAl are given in Refs. [6,26–31]. They are calculated at a mean temperature in each zone. In the reaction zone, the properties of particles are equal to the average of their respective values of the reactant and product species. The properties of the mixture in the preheat and reaction zones are averaged, respectively, to obtain the mean properties of the pellet. To facilitate comparison with experimental data [13], the particle size is chosen as 79 μm.

2.1. Energy balance

The experimental setup for nickel-coated aluminum particles does not include an enclosing surface [13]. The energy conservation takes the form [32]:

$$\rho_m C_{p,m} \frac{\partial T}{\partial t} = \lambda_m \frac{\partial^2 T}{\partial x^2} + \dot{Q}_{gen} - \dot{Q}_{conv} - \dot{Q}_{rad}, \tag{1}$$

where ρ is the density, C_p the specific heat, T the temperature, t the time, λ the thermal conductivity, x the spatial coordinate, $\dot{Q}_{gen}$ the heat generation rate, and $\dot{Q}_{conv}$ and $\dot{Q}_{rad}$ are the rates of heat loss by convection and radiation, respectively, to the ambiance. The subscript m refers to the mixture. The heat generation rate, $\dot{Q}_{gen}$, is expressed as

$$\dot{Q}_{gen} = \rho_m Q_r \dot{\omega}, \tag{2}$$

where Q_r is the heat of reaction and $\dot{\omega}$ the reaction rate. The rates of heat loss by convection and radiation from the pellet to the ambient gas are given by

$$\dot{Q}_{conv} = \frac{4h}{D}(T - T_a), \tag{3}$$

$$\dot{Q}_{rad} = \frac{4\varepsilon\sigma}{D}(T^4 - T_a^4) \tag{4}$$

where D is the pellet diameter (=6.35 mm) [13], $\varepsilon = 0.25$ the particle emissivity [33], σ the Stefan–Boltzmann constant. The subscript a refers to the ambient environment. Based on the Nusselt number correlation reported in Ref. [34], the heat transfer coefficient, h, is calculated to be 19.68 W/m² K.

The following initial and boundary conditions are specified to close the formulation:

$$\begin{aligned} t = 0 &: T = T_u, \\ x = 0 &: T = T_f, \\ x = L &: \frac{\partial T}{\partial x} = 0, \end{aligned} \tag{5}$$

where L = 6.35 mm is the pellet length. The subscript f refers to the flame. The energy equation is solved numerically by an explicit finite difference method. The grid size and time step are chosen as 12.7 μm and 10 ns, respectively. Negligible improvement in the results is obtained when a smaller grid size or a lower time step is employed. The temperature of the first grid point (x = 0) is taken to be equal to the adiabatic flame temperature of nickel–aluminum system (1911 K) [32].

The ignition temperature and burning time must be specified as input parameters in the present analysis. Dean et al. [13] conducted differential scanning calorimetry (DSC) testing of 79 μm nickel-coated aluminum particles. The samples were heated in an argon atmosphere at a rate of 20 °C/min. For uniaxially pressed pellets, reactions began upon melting of aluminum at 933 K. The cold sprayed sample, however, exhibited reactivity at a lower temperature of ~800 K. For simplicity, the ignition temperature is taken to be 933 K in the present analysis. Note that reactions may occur at temperatures lower than the melting point of aluminum, depending on the microstructure and morphology of the materials, heating rate, ambient conditions, and composition ([18,19]). Furthermore, at higher loading densities, the oxide layer could be damaged during compaction. As a result, the actual ignition temperature could be lower than the melting point of aluminum (933 K), especially for dense mixtures.

The reaction mechanism of nickel-coated aluminum particles is not well understood. Thiers et al. [12] studied the reactivity of nickel-coated aluminum powder compacts under a thermal explosion mode. The core diameter was in the range of 40–60 μm and shell thickness of 2–3 μm was considered. Cracking of the nickel shell and ejection of aluminum atoms were observed. Shteinberg et al. [35] measured the reaction kinetics of nickel-coated aluminum particles of diameter 30–40 μm using an electro-thermal analysis. The burning process was divided into three stages based on the measured activation energies. In the first stage, the particle was heated from 1113 to 1250 K, due to dissolution of nickel atoms. The corresponding activation energy was 50 kcal/mol. The second stage (1250–1400 K) was marked by cracking of the oxide layer and ejection of molten aluminum. In the third stage, changes in reaction mechanism resulted in a significantly higher activation energy of 125 kcal/mol. White et al. [36] conducted a similar

Table 2
Thermophysical properties of different species in preheat and reaction zones.[a]

Species	Thermal conductivity (W/m K)		Specific heat (J/kg K)		Density (kg/m³)		Melting point (K)	
	P	R	P	R	P	R	P	R
Al	220	130	1060	1176	2700		933	
Ni	66	80	440	670	8908		1728	
NiAl alloy	–	115	–	717	5900		1910	
Ni-coated Al	137	108	613	760	5430		–	
Ar	0.016	0.055	520	520	0.89	0.37	–	

P: preheat zone; R: reaction zone.
[a] Particle diameter is 79 μm, Ni shell thickness is 7 μm, and gas pressure is 1 atm.

thermal analysis. The measured overall activation energy of 30–40 µm nickel-coated aluminum particles was 84 kcal/mol, which falls into the range reported by Shteinberg et al. [35]. Andrzejak et al. [2] investigated the ignition of isolated nickel-coated aluminum particles of diameter ~2.5 mm. The shell thickness varied in the range of 7.6–147 µm. The proposed mechanism involves dissolution of nickel atoms and formation (and melting) of various Ni–Al species at the interface. Recent MD simulations by Sundaram et al. [3] and Henz et al. [17] predict the diffusion and mixing of nickel and aluminum atoms. The fragmentation of the nickel shell was considered by Delogu [16]. For simplicity, the reaction rate is assumed to be controlled by species diffusion processes. The burning time (t_b) of particles [37] can be expressed as

$$t_b = \dot{\omega}^{-1} = \frac{r^2}{cD},$$
(6)

where r is the core radius, D the diffusion coefficient, and c the burning-time constant. According to the Einstein–Smoluchowski equation, the constant c is equal to six for three-dimensional systems [37]. It may, however, be treated as an adjustable parameter to accommodate the effects of several poorly understood phenomena, such as temporal variations in the heat-release rate, cracking of the shell due to core melting, and/or compaction, and ensuing changes in the reaction mechanism. Alternatively, the following reaction rate model [38] may be considered:

$$\dot{\omega} = \frac{d\eta}{dt} = K_0(1 - \eta) \exp\left(\frac{-E_A}{RT}\right),$$
(7)

where η is the fraction of the burned reactants, K_0 the frequency factor, and E_A the activation energy. For nickel-coated aluminum particles, the activation energy is measured to be in the range of 50–150 kcal/mol ([35,36]), and the frequency factor should be treated as an adjustable parameter. Calculations indicate that K_0 varies in the range of 10^7–10^{13} s^{-1}, depending on the chosen activation energy.

2.2. Thermal conductivity

Thermo-physical properties are of paramount importance in predicting the burning properties. The thermal conductivity of nickel-coated aluminum particles, λ_p, is a function of the core diameter and shell thickness. It is calculated as follows [39]:

$$\lambda_p = \frac{\lambda_{Al}^2 R}{(r - R)[2\lambda_{Al} \ln a - 2\lambda_{Ni} \ln a - (\lambda_{Al}^2/\lambda_{Ni})] + r\lambda_{Al}}$$
(8)

where

$$a \equiv \frac{b - \lambda_{Al} R}{b - \lambda_{Al}(R - r)}; b \equiv 2(R - r)\lambda_{Ni} + 2r\lambda_{Al}.$$
(9)

Here λ stands for the thermal conductivity, r the radius of the Al core, R the outer radius of the particle. The subscripts Al, Ni, and p refer to aluminum, nickel, and particle, respectively. Several correlations are available in the literature for calculating the effective thermal conductivity of multi-phase mixtures. The following benchmark models are considered in the present study.

Parallel

$$\lambda_m = \phi_p \lambda_p + \phi_f \lambda_f;$$
(10)

where ϕ stands for the volume fraction. The subscript f denotes fluid.

Maxwell–Eucken [40–42]

$$\lambda_m = \frac{\phi_f \lambda_f + \phi_p \lambda_p \left(\frac{3\lambda_f}{2\lambda_f + \lambda_p}\right)}{\phi_f + \phi_p \left(\frac{3\lambda_f}{2\lambda_f + \lambda_p}\right)};$$
(11)

Ticha et al. [43]

$$\lambda_m = \lambda_p \exp\left(-\frac{1.5\phi_f}{1 - \phi_f}\right);$$
(12)

Bruggeman [40,44]

$$\phi_p \left(\frac{\lambda_p - \lambda_m}{\lambda_p + 2\lambda_m}\right) + \phi_f \left(\frac{\lambda_f - \lambda_m}{\lambda_f + 2\lambda_m}\right) = 0;$$
(13)

Eq. (13) can be solved to obtain the following expression for thermal conductivity:

$$\lambda_m = \frac{\lambda_f}{4} \left[(3\phi_p - 1)\frac{\lambda_p}{\lambda_f} + (2 - 3\phi_p) + \sqrt{\Delta}\right];$$

$$\Delta = \left(\frac{\lambda_p}{\lambda_f}\right)^2 (3\phi_p - 1)^2 + (2 - 3\phi_p)^2 + \frac{2\lambda_p}{\lambda_f}(2 + 9\phi_p - 9\phi_p^2).$$
(14)

The parallel model is based on simple volume averaging of the properties of the two phases, assuming that the layers of the components are aligned parallel to the heat flow. According to the Maxwell–Eucken model, the particles are greatly dispersed and their interactions are neglected. Bruggeman's theory, on the other hand, assumes random distribution of the individual components. Ticha et al.'s expression [43] was obtained for materials with internal porosities.

In real materials, the interactions between particles cannot be neglected, especially at high particle loading densities. Furthermore, the distribution of constituent materials in a multi-phase mixture is not completely random. It is thus important to unify the Maxwell–Eucken and Bruggeman theories. The methodology developed by Wang et al. [40] has been adopted in the present study. The complex material structure is approximated as a mixture of Bruggeman and Maxwell–Eucken structures. The thermal conductivity of the mixture is given by [40]

$$\lambda_m = \frac{D + \sqrt{D^2 + 2\lambda_p \lambda_f}}{2},$$

$$D = (2\lambda_p - \lambda_f)\phi_p(1 - \alpha_{p,1}) + (2\lambda_f - \lambda_p)\phi_f \left(\frac{2\phi_f + 2\phi_p \alpha_{p,1} - 1}{2\phi_f}\right),$$
(15)

where ϕ is the component volume fraction and α the volume fraction of each component with a specified structure. The subscript 1 refers to the Maxwell–Eucken structure. The thermal conductivity is determined iteratively, since the parameter $\alpha_{p,1}$ is not known *a priori*. Figure 2 shows the effect of particle volume fraction on the fractions of fluid and particle phases with the Maxwell–Eucken structure for various ratios of thermal conductivity. The parameter $\alpha_{p,1}$ increases with increasing particle volume fraction, reaches a maximum value, and decreases with further increase in the volume fraction. Note that the particle volume fraction corresponding to the peak value of $\alpha_{p,1}$ is greater for a mixture with a higher thermal conductivity ratio. The parameter $\alpha_{f,1}$, on the other hand, decreases monotonically with increasing volume fraction of the particles. For a thermal conductivity ratio of 2000, $\alpha_{f,1}$ is negligibly small for volume fractions exceeding 0.65. Note that the thermal conductivity of the mixture is equal to that of particle in the limit of vanishing $\alpha_{f,1}$. Figure 3 shows the variation of effective thermal conductivity with particle volume fraction for various thermal conductivity ratios. For $\lambda_p/\lambda_f = 20$, the effective thermal conductivity increases gradually toward the maximum value. A sharp increase at $\phi_p = 0.65$ is, however, observed for $\lambda_p/\lambda_f = 2000$. For lower volume fractions, the thermal conductivity of the mixture is nearly equal to that fluid. Note that such a high thermal conductivity ratio is
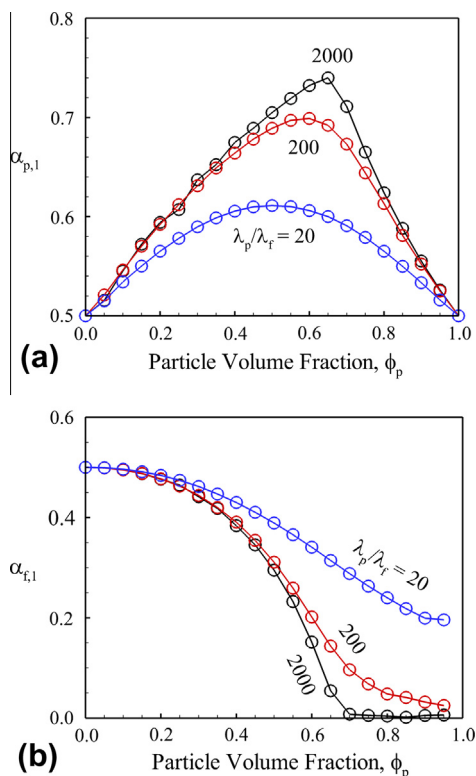
Fig. 2. Effect of particle volume fraction on the fractions of fluid and particle phases with Maxwell–Eucken structure for various ratios of thermal conductivities.
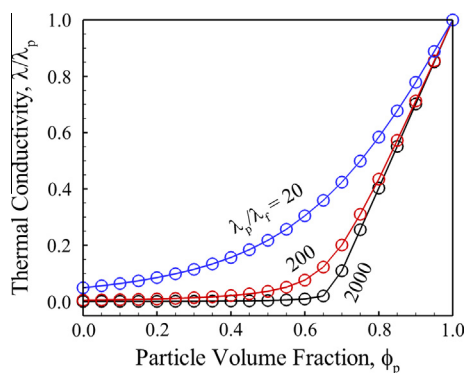

Fig. 3. Variation of effective thermal conductivity with particle volume fraction for different ratios of thermal conductivities; Maxwell–Eucken–Bruggeman model.
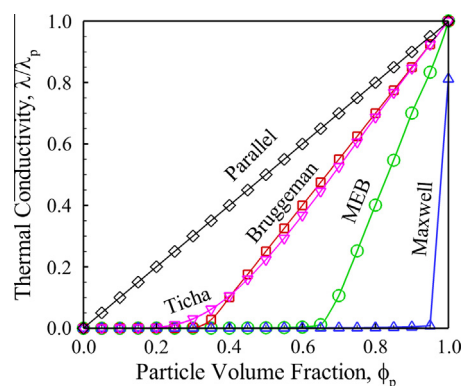

Fig. 4. Variations of thermal conductivity with particle volume fraction as predicted by different models.

representative of conditions encountered in the present study, in which gaseous argon is seeded with highly conducting metallic particles.

Figure 4 shows a comparison of the predictions of the Maxwell–Eucken–Bruggeman (MEB) model with the other models considered in the present study. The Parallel model predicts a linear dependence of the thermal conductivity on the particle volume fraction. The Maxwell model, on the other hand, suggests that the thermal conductivity is constant up to a volume fraction of 0.95. Since the Maxwell analysis does not treat particle–particle interactions, the results are not expected to be accurate for large particle volume fractions. The models of Ticha et al. and Bruggeman produce almost identical results, with a sharp increase in the thermal conductivity at a volume fraction of 0.3. The former expression is much simpler and has been employed in the combustion analysis of metal–water systems [45,46].

2.3. Diffusion coefficient

The diffusion coefficient must be specified as an input parameter in the present analysis. It takes the form

$$D = D_0 \exp(-E_A/RT), \tag{16}$$

where $D_0 = 9.54$ Å^2/ps is the pre-exponential constant and $E_A = 26$ kJ/mol the activation energy [47]. Several other researchers have obtained the diffusivities of the Ni–Al system [48–51] and significant disparities exist between the values in the literature. For example, the diffusivities obtained by Alawieh et al. [49] are at least an order of magnitude lower than those of Du et al. [47]. Further studies are warranted. Note that the diffusion coefficient at a specified temperature may not be a constant during mixing due to the formation of inter-metallic phases [51].
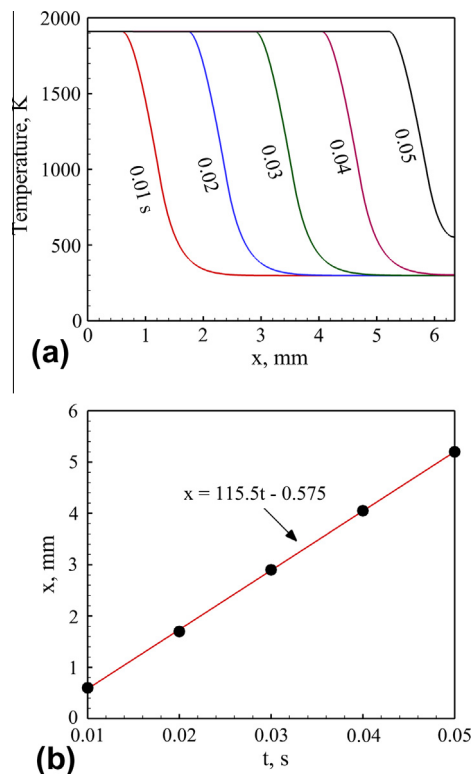

Fig. 5. (a) Time evolution of temperature distribution in a pellet of nickel-coated aluminum particles (b) position of the flame front as a function of time; particle loading density of 100%.

3. Results and discussion

The theoretical framework described in Section 2 is employed to analyze the flame structure and burning rate of nickel-coated aluminum particles for a wide range of pellet densities. The particle diameter is 79 μm and shell thickness is 7 μm. The aluminum content is 27.8 wt.%. Figure 5 shows the temperature distribution in a pellet of nickel-coated aluminum particles for a loading density of 100%. The temperature increases from the initial value of 298 K in the preheat region and attains a maximum value of ~1900 K. Note that the reaction temperature is approximately equal to the adiabatic flame temperature of an equimolar nickel–aluminum system (i.e., 1910 K [6]). The burning rate is determined using a curve fit to position vs. time, as shown in the figure. The model predicts the burning process to be steady, which is in reasonable agreement with experimental data. The actual velocity of the flame front is strictly not constant throughout the burning process, due to the presence of density gradients in the pellet and degassing of the particles [13]. These phenomena could be considered in a more comprehensive model in order to describe the temporal variations of the burning rate. It should be noted that the measured burning rates were obtained using a curve-fit to the flame position vs. time. The coefficients of determination of these fits were greater than 0.95 for all loading densities [13].

Thermal conductivity plays a critical role in dictating the pellet burning behaviors. Figure 6 shows the variation of the burning rate with the pellet density based on five different thermal conductivity models. For the parallel model, the thermal conductivity varies lin-
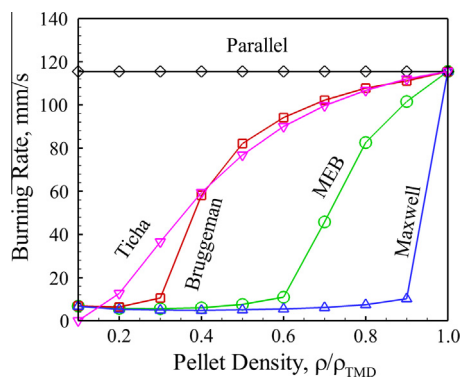
Fig. 6. Effect of particle loading density on burning rate of nickel-coated aluminum particles using different thermal conductivity models; particle diameter is 79 μm and nickel shell thickness is 7 μm.
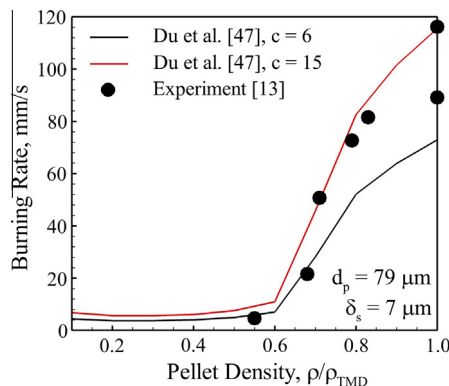
Fig. 7. Effect of particle loading density on burning rate of nickel-coated aluminum particles; thermal conductivity calculated using the Maxwell–Eucken–Bruggeman model; particle diameter is 79 μm and nickel shell thickness is 7 μm.
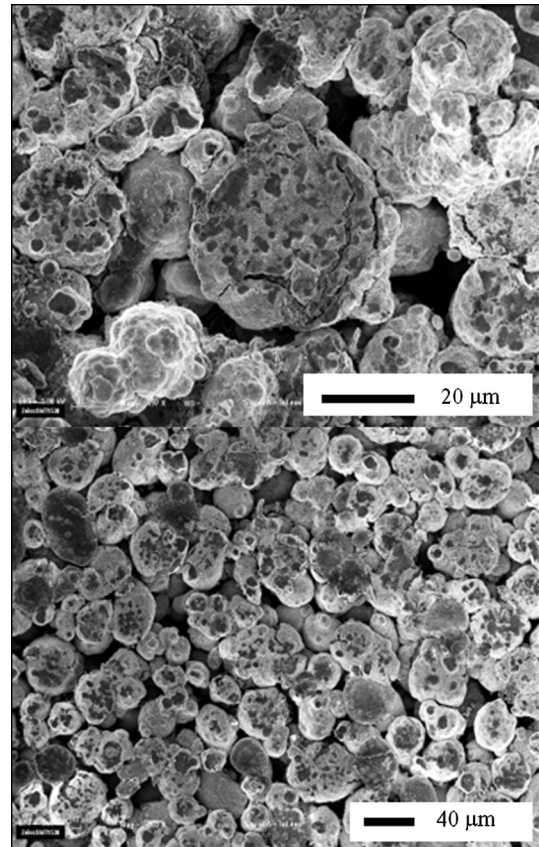
Fig. 8. Scanning electron micrographs of pellets containing nickel-coated aluminum particles (a) mean particle diameter of 49 μm and loading density of 80% (b) mean particle diameter of 79 μm and loading density of 70% (courtesy of Mr. Steven Dean and Dr. Richard Yetter).

early with the pellet density. As a result, the effects of thermal conductivity and density counteract each other, leading to a constant burning rate. The Maxwell model gives rise to a burning rate which remains nearly constant up to a density of 90% and then increases sharply toward the maximum value. The models of Bruggeman and Maxwell–Eucken–Bruggeman, on the other hand, indicate that the burning rate increases suddenly at loading densities of 30% and 60%, respectively. The model of Ticha et al. significantly under-predicts the burning rate for packing densities lower than 20%. The above results clearly indicate that heat transport in a heterogeneous system must be treated properly, so that burning rates can be accurately predicted for all loading densities.

Figure 7 shows the burning rate calculated using the Maxwell–Eucken–Bruggeman model. Reasonably good agreement with experimental data [13] is achieved. This thermal conductivity model offers the best predictions for a packing density in the range of 10–100%. For a loading density of 100%, the model predicts a burning rate of ~70 mm/s when the parameter c is taken to be six. This is lower than the experimental data by about 20%. This is more so should the diffusion coefficients of Alawieh et al. [49] be employed. Better agreement with experimental data is achieved when the burning-time constant is greater than six. Further studies elucidating the diffusion process in a pellet of nickel-coated aluminum particles is warranted. Carson et al. [52] define the thermal conductivity bounds for various heterogeneous systems. For systems in which the thermal conductivity of the dispersed phase is lower than that of the continuous phase (such as gas-filled internal pores in a solid matrix), the effective thermal conductivity is greater than the predictions of the Bruggeman model. For other cases (such as metal particles

dispersed in fluids), the effective thermal conductivity is bounded by the limits prescribed by the Maxwell–Eucken and Bruggeman models. The Maxwell–Eucken model assumes that the particles are dispersed and do not form a continuous medium. The Bruggeman model, on the other hand, treats random distribution of the components.

Figure 8 shows scanning electron micrographs of nickel-coated aluminum pellets at loading densities of 70% and 80%. It is apparent that the particles are in close contact at several instances. As a result, the Maxwell–Eucken model is not expected to give accurate predictions for these loading densities. The distribution of components is also not completely random. The Maxwell–Eucken–Bruggeman model is thus more suitable for heterogeneous systems such as particle-laden fluids. It is interesting to note that a qualitatively similar trend was observed for aluminum–molybdenum trioxide (Al/MoO$_3$) pellets [53]. The diameter of aluminum particles is 3–4 μm and the MoO$_3$ powder consists of rectangular particles with thickness on the order of 5–10 nm and lengths varying from 0.5–1.0 μm. The initial temperature is 298 K and pressure is 1 atm. The burning rate remained nearly constant at ∼1 m/s for loading densities lower than 50% and increases sharply toward a value of ∼40 m/s at a loading density of 70%. Note, however, that Al/MoO$_3$ is a gas-generating system and convective propagation is likely to occur, especially for lower packing densities. As a result, the effect of gas generation on the burning rate must be considered to facilitate comparison with experimental data. For pellets containing separate nickel and aluminum particles, the burning rate decreases with increasing pellet density [13]. Optical micrographs indicate that the nickel particles have agglomerated significantly [13], thereby hampering the interactions between nickel and aluminum atoms. As a result, it is likely that the reaction rate decreases with increasing loading density. For nickel-coated aluminum particles, the core–shell structure helps to preserve the interface for all particle loading densities. The variation of the burning rate with pellet density is thus only attributed to the changes in the thermal diffusivity of the mixture.

For a particle size of 79 μm, the maximum burning rate is calculated to be 115 mm/s. An analytical expression for the burning rate can be obtained following the approach of Zeldovich, Frank-Kamenetskii, and Semenov [54]

$$r_b = \sqrt{\frac{\lambda_m}{\rho C_p} \frac{Q_m}{C_p(T_{ign} - T_u)} \dot{\omega}}. \tag{17}$$

Eq. (17) yields a value of 122.8 mm/s for the burning rate at a loading density of 100%, which agrees reasonably well with the results of the present analysis. The model of Zeldovich et al. assumes that the propagation of the combustion wave is driven by the heat conduction from the flame zone to the unburned region.

It is important to analyze the effect of radiation on the burning rate. The optical thickness of the medium is calculated as

$$l_o = \beta^{-1} = \frac{2\rho_p d_p}{3\phi_p \rho_m (Q_a + Q_s)}, \tag{18}$$

where l_o is the optical thickness, β the extinction coefficient, Q_s the scattering efficiency, and Q_a the absorption efficiency. The size parameter ($\pi d_p/\lambda$) is of the order of 100, indicating that the particle diameter is significantly greater than the wavelength of thermal radiation. Under such conditions, the absorption and scattering efficiencies, Q_a and Q_s, can be expressed respectively as [55]

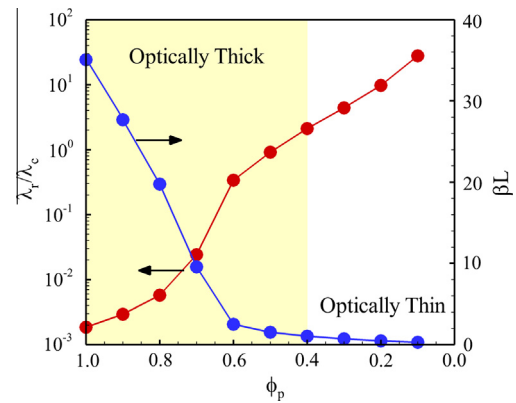$$Q_a = 2(1 - A)G(B) \tag{19}$$

$$Q_s = 2 - Q_a \tag{20}$$

Fig. 9. Effect of particle volume fraction on optical thickness and radiative thermal conductivity of nickel-coated aluminum particles; particle diameter is 79 μm and nickel shell thickness is 7 μm.

where

$$A = R + (A - 1)\exp(-B), \tag{21}$$

$$B = \frac{2n(1 + 2/(n^2 + k^2))}{1 - A}, \text{ and} \tag{22}$$

$$R = \frac{(n - 1)^2 + k^2}{(n + 1)^2 + k^2}. \tag{23}$$

The function G takes the form

$$G(x) = \frac{1}{2} + \frac{e^{-x}}{x} + \frac{e^{-x} - 1}{x^2}, \tag{24}$$

where n and k are the real and imaginary parts of the refractive index, respectively. For a wavelength of 1 μm, n and k are equal to 3 and 5, respectively. Eq. (18) can then be used to calculate the optical thickness for various loading densities. For optically thick conditions ($\beta L > 1$), the diffusion approximation can be invoked. The radiative thermal conductivity is given by [56]

$$\lambda_r = \frac{16\sigma n^2 T^3}{3\beta}, \tag{25}$$

where σ is the Stefan–Boltzmann constant. Figure 9 shows the effect of the particle volume fraction on the optical thickness and radiative thermal conductivity for a pellet of nickel-coated aluminum particles. For loading densities greater than 40%, the medium is optically thick. In this regime, the calculated radiative thermal conductivity is orders of magnitude lower than the conduction counterpart. The flame propagation is dictated by heat conduction; the assumption invoked in the present study is thus justified. Note that the diffusion approximation is not valid for optically thin conditions. It over-predicts the radiative thermal conductivity for loading densities lower than 40%. A more sophisticated analysis considering a complete radiative transport equation is required to elucidate the effect of thermal radiation on the burning behavior for optically thin conditions. The present analysis does, however, capture the main features of combustion of nickel-coated aluminum particles, with reasonably good agreement between the predictions and experimental data.

4. Conclusions

A theoretical analysis was conducted to investigate the flame propagation characteristics of nickel-coated aluminum particles for packing densities in the range of 10–100% of the theoretical maximum density. Emphasis was placed on the effect of packing

density on the burning properties of nickel-coated aluminum particles. The energy conservation equation was solved numerically and the burning rate was determined from the temporal variations of the position of the flame front. The diffusion coefficients and reaction rate of nickel-coated aluminum particles were incorporated into the flame propagation analysis. As a specific example, the case with a particle size of 79 μm was considered. Of the five different thermal conductivity models considered in the present work, the Maxwell–Eucken–Bruggeman model offered the best predictions of the burning rate for all loading densities. The burning rate remained nearly constant (<1 cm/s) up to a density of 60% and then increased sharply toward the maximum value of 11.55 cm/s at a density of 100%. Radiation heat transfer exerted a negligible effect on the burning behaviors for packing densities greater than 40%. A more sophisticated analysis considering a complete radiative transport equation is required to elucidate the effect of thermal radiation on burning behavior for optically thin conditions.

Acknowledgments

References

[1] E. Shafirovich, A. Mukasyan, L. Thiers, A. Varma, B. Legrand, C. Chauveau, I. Gokalp, Combust. Sci. Technol. 174 (2002) 125–140.
[2] T.A. Andrzejak, E. Shafirovich, A. Varma, Combust. Flame 150 (2007) 60–70.
[3] D.S. Sundaram, P. Puri, V. Yang, J. Phys. Chem. C 117 (2013) 7858–7869.
[4] D.A. Yagodnikov, A.V. Voronetskii, Combust. Expl. Shock Waves 33 (1997) 49–55.
[5] T.J. Foley, C.E. Johnson, K.T. Higa, Chem. Mater. 17 (2005) 4086–4091.
[6] K. Morsi, Mater. Sci. Eng. 299 (2001) 1–15.
[7] A. Varma, A.S. Rogachev, A.S. Mukasyan, S. Hwang, Adv. Chem. Eng. 24 (1998) 79–226.
[8] P. Zhu, J.C.M. Li, C.T. Liu, Mater. Sci. Eng. 357 (2003) 248–257.
[9] T.S. Dyer, Z.A. Munir, Metall. Mater. Trans. B 26 (1995) 603–610.
[10] E.M. Hunt, K.B. Plantier, M.L. Pantoya, Acta Mater. 52 (2004) 3183–3191.
[11] P. Zhu, J.C.M. Li, C.T. Liu, Mater. Sci. Eng. 329 (2002) 57–68.
[12] L. Thiers, A.S. Mukasyan, A. Varma, Combust. Flame 131 (2002) 198–209.
[13] S.W. Dean, J.K. Potter, R.A. Yetter, T.J. Eden, V. Champagne, M. Trexler, Intermetallics 43 (2013) 121–130.
[14] R.V. Reeves, A.S. Mukasyan, S.F. Son, J. Phys. Chem. C 114 (2010) 14772–14780.
[15] F. Baras, O. Politano, Phys. Rev. B 84 (2011) 024113.
[16] F. Delogu, Nanotechnology 18 (2007) 505702.
[17] B.J. Henz, T. Hawa, M.R. Zachariah, J. Appl. Phys. 105 (2009) 124310.
[18] P. Swaminathan, M.D. Grapes, K. Woll, S.C. Barron, D.A. LaVan, T.P. Weihs, J. Appl. Phys. 113 (2013) 143509.
[19] J.C. Crone, J. Knap, P.W. Chung, B.M. Rice, Appl. Phys. Lett. 98 (2011) 141910.
[20] T.S. Dyer, Z.A. Munir, V. Ruth, Scripta Mater. 10 (1994) 1281–1286.
[21] I.E. Gunduz, K. Fadenberger, M. Kokonou, C. Rebholz, C.C. Doumanidis, Appl. Phys. Lett. 93 (2008) 134101.
[22] R. Knepper, M.R. Snyder, G. Fritz, K. Fisher, O.M. Knio, T.P. Weihs, J. Appl. Phys. 105 (2009) 083504.
[23] H.P. Li, J.A. Sekhar, J. Mater. Res. 10 (1995) 2471–2480.
[24] G.M. Fritz, H. Joress, T.P. Weihs, Combust. Flame 158 (2011) 1084–1088.
[25] S.C. Saxena, High Temp. Sci. 3 (1971) 168–188.
[26] Y. Terada, K. Ohkubo, T. Mohri, T. Suzuki, Mater. Trans. 43 (2002) 3167–3176.
[27] W.F. Gale, T.C. Totemeier, Smithells Metals Reference Book, eighth ed., Elsevier, 2004.
[28] J.F. Shackelford, W. Alexander, Materials Science and Engineering Handbook, third ed., CRC Press, 2001.
[29] E.H. Buyco, F.E. Davis, J. Chem. Eng. Data 15 (1970) 518–523.
[30] V. Recoules, J.P. Crocombette, Phys. Rev. B 72 (2005) 104202.
[31] M.W. Chase Jr., NIST-JANAF Thermochemical Tables, fourth ed., 1998.
[32] H.P. Li, Mater. Chem. Phys. 80 (2003) 758–767.
[33] G. Teodorescu, Radiative Emissivity of Metals and Oxidized Metals at High Temperature, Ph.D. Thesis, Auburn University, 2007.
[34] J.C. Day, M.K. Zemler, M.J. Traum, S.K.S. Boetcher, J. Heat Transfer 135 (2013) 022505.
[35] A.S. Shteinberg, Y.C. Lin, S.F. Son, A.S. Mukasyan, J. Phys. Chem. A 114 (2010) 6111–6116.
[36] J.D.E. White, R.V. Reeves, S.F. Son, A.S. Mukasyan, J. Phys. Chem. A 113 (2009) 13541–13547.
[37] A. Felinger, J. Chromatogr. A 1218 (2011) 1939–1941.
[38] J.J. Moore, H.J. Feng, Prog. Mater. Sci. 39 (1995) 275–316.
[39] B. Badrinarayan, J.W. Barlow, Proc. Solid Freeform Fabrication (1990) 91–97.
[40] J. Wang, J.K. Carson, M.F. North, D.J. Cleland, Int. J. Heat Mass Transfer 49 (2006) 3075–3083.
[41] J.C. Maxwell, A Treatise on Electricity and Magnetism, Dover Publications Inc., New York, 1954.
[42] A. Eucken, Fors. Gabiete Ing. 11 (1940) 6–20.
[43] G. Ticha, W. Pabst, D.S. Smith, J. Mater. Sci. 40 (2005) 5045–5047.
[44] D.A.G. Bruggeman, Ann. Phys. 24 (1935) 636–664.
[45] D.S. Sundaram, V. Yang, Y. Huang, G.A. Risha, R.A. Yetter, Combust. Flame 160 (2013) 2251–2259.
[46] M. Diwan, D. Hanna, E. Shafirovich, A. Varma, Chem. Eng. Sci. 65 (2010) 80–87.
[47] Y. Du, Y.A. Chang, B. Huang, W. Gong, Z. Jin, H. Xu, Z. Yuan, Y. Liu, Y. He, F.Y. Xie, Mater. Sci. Eng. 363 (2003) 140–151.
[48] M.J. Cherukara, K.G. Vishnu, A. Strachan, Phys. Rev. B 86 (2012) 075470.
[49] L. Alawieh, T.P. Weihs, O.M. Knio, Combust. Flame 160 (2013) 1857–1869.
[50] A.B. Mann, A.J. Gavens, M.E. Reiss, D. Van Heerden, G. Bao, T.P. Weihs, J. Appl. Phys. 82 (1997) 1178.
[51] R.G. Xu, M.L. Falk, T.P. Weihs, J. Appl. Phys. 114 (2013) 163511.
[52] J.K. Carson, S.J. Lovatt, D.J. Tanner, A.C. Cleland, Int. J. Heat Mass Transfer 48 (2005) 2150–2158.
[53] M. Pantoya, V.I. Levitas, J.J. Granier, J.B. Henderson, J. Prop. Power 25 (2009) 465–470.
[54] I. Glassman, Combustion, first ed., Academic Press, 1977. pp. 68–75.
[55] P.H. Levine, Appl. Opt. 17 (1978) 3861–3862.
[56] R. Siegel, J.R. Howell, Thermal Radiation Heat Transfer, Hemisphere, 1981.